

Efficient B-mode Ultrasound Image Reconstruction from Sub-sampled RF Data using Deep Learning

Yeo Hun Yoon, Shujaat Khan, Jaeyoung Huh, and Jong Chul Ye, *Senior Member, IEEE*

Abstract—In portable, three dimensional, and ultra-fast ultrasound imaging systems, there is an increasing demand for the reconstruction of high quality images from a limited number of radio-frequency (RF) measurements due to receiver (Rx) or transmit (Xmit) event sub-sampling. However, due to the presence of side lobe artifacts from RF sub-sampling, the standard beam-former often produces blurry images with less contrast, which are unsuitable for diagnostic purposes. Existing compressed sensing approaches often require either hardware changes or computationally expensive algorithms, but their quality improvements are limited. To address this problem, here we propose a novel deep learning approach that directly interpolates the missing RF data by utilizing redundancy in the Rx-Xmit plane. Our extensive experimental results using sub-sampled RF data from a multi-line acquisition B-mode system confirm that the proposed method can effectively reduce the data rate without sacrificing image quality.

Index Terms—Ultrasound imaging, B-mode, multi-line acquisition, deep learning, Hankel matrix

I. INTRODUCTION

DUE to the excellent temporal resolution with reasonable image quality and minimal invasiveness, ultrasound (US) imaging has been adopted as a golden-standard for the diagnosis of many diseases in the heart, liver, etc. Accordingly, there have been many research efforts to extend US imaging to new applications such as portable imaging in emergency care [2], 3-D imaging [3], ultra-fast imaging [4], [5], etc.

To achieve better spatial resolution in US imaging, high-speed analog-to-digital converters (ADC) should be used for the Rx portion of the US transducer, which consumes significant power. Accordingly, in portable US systems, a small number of Rx elements with reduced aperture sizes are used to reduce power consumption, which often results in the deterioration of image quality. On the other hand, to achieve higher frame rates, the number of transmit events should be reduced, as the duration of the transmit event is determined by the speed of sound. This in turn leads to down-sampling artifacts.

To address these problems, compressed sensing (CS) approaches have been investigated [6]–[10]. However, US specific properties often deteriorate the performance of CS approaches. For example, due to the wave nature of ultrasound

scattering, it is often difficult to accurately model the sensing matrix. Moreover, US images contain characteristic speckles, which make them barely sparse in any basis. Instead of using wave scattering physics, Wagner *et al.* [8] modeled a scan line profile as a signal with a finite rate of innovations (FRI) [11], and proposed a specially designed hardware architecture that enables high-resolution scan line reconstruction [8]. One of the drawbacks of this approach, however, is that it cannot be used for conventional B-mode imaging systems.

Recently, inspired by the tremendous success of deep learning in classification [12]–[14] and low-level computer vision problems [15]–[17], many researchers have investigated deep learning approaches for various biomedical image reconstruction problems and successfully demonstrated significant performance improvements over CS approaches [18]–[30]. The source of deep learning success in image reconstruction lies in its exponentially increasing expressiveness, which can capture modality-specific image features [31]. Therefore, this paper aims at developing a deep learning algorithm that provides efficient image reconstruction from sub-sampled RF data.

In US literature, the works in [32], [33] were among the first to apply deep learning approaches to US image reconstruction. In particular, Allman *et al* [32] proposed a machine learning method to identify and remove reflection artifacts in photoacoustic channel data. Luchies and Byram [33] proposed an ultrasound beam-forming approach using deep neural networks. These works were more focused on processing fully-sampled channel RF data than reconstruction from sub-sampled channel RFs. To the best of our knowledge, no existing deep learning approaches address image recovery from channel RF sub-sampled data.

One of the most important contributions of this work is that it demonstrates that deep neural networks can estimate missing RF data from Rx and/or Xmit event subsampling without sacrificing image quality. However, a deep neural network is usually considered a black box, so its application to medical image reconstruction often causes skepticism as to whether the enhancement is cosmetic or real. Thus, in contrast to common practice, our deep neural network is carefully designed based on theoretical justification. More specifically, our earlier work [34] showed that strong correlation in RF data results in a rank deficient Hankel structured matrix so that missing RF data can be estimated using an annihilating filter-based low rank Hankel matrix approach (ALPHA) [35]–[39]. In another of our group’s previous works [40], we discovered that deep neural networks are closely related to low-rank Hankel matrix decomposition using data-driven convolutional framelets. By synergistically combining these findings, we propose a deep

Copyright (c) 2017 IEEE. Personal use of this material is permitted. However, permission to use this material for any other purposes must be obtained from the IEEE by sending a request to pubs-permissions@ieee.org.

The authors are with the Department of Bio and Brain Engineering, Korea Advanced Institute of Science and Technology (KAIST), Daejeon 34141, Republic of Korea (e-mail: {caffemocha,shujaat,woori93,jong.ye}@kaist.ac.kr). Parts of this work was presented in 2018 IEEE International Conference on Acoustic, Speech and Signal Processing (ICASSP) [1]. Code and dataset is available at https://github.com/BISPL-JYH/Ultrasound_TMI.

neural network that performs direct RF data interpolation by exploiting RF data redundancy in a fully data-driven manner.

In addition to the theoretical justification, there are several benefits from our approach. First, in contrast to the low-rank matrix completion approach for RF interpolation [34], our deep network has a run-time complexity that is several orders of magnitude lower. However, it is important to note that the proposed neural network is not another implementation of ALOHA for computational saving; rather, it is a new algorithm that significantly improves the interpolation performance of ALOHA by exploiting the exponential expressiveness of a deep neural network as confirmed later by extensive experimental results.

Another important benefit to exploiting the link between ALOHA and the deep neural network is that it guides us to choose an appropriate domain to implement a deep neural network. Since ALOHA successfully interpolated RF data in our prior work [34], our theoretical understanding of the link led us to implement a neural network in the RF domain, which may be unexpected from the perspective of implementing a standard deep neural network. Compared to image domain CNNs that attempt to learn acquisition geometry specific artifacts, one of the most important advantages of the proposed RF domain CNN is its generalization power. For example, although an image domain deep learning approach requires many sets of data from different acquisition geometries and body areas [18], our CNN can be trained using RF data measured by a specific transducer for a particular organ, but it can also be used for other types of transducers and/or different organs.

The rest of the paper is organized as follows. Section II reviews the B-mode US acquisition physics. In Section III, we explain the inherent redundancy in RF data, and how it can be exploited using a deep neural network. Experimental methods and results are presented in Section IV and Section V, which is followed by the conclusions in Section VI.

II. IMAGING PHYSICS

A. B-mode Ultrasound Imaging

B-mode ultrasound imaging, which is most widely used in practice, scans the body using focused beams and reconstruct 2-D images as shown in Fig. 1. Here, X_{mit} , Rx, and DAS denote the transmit event for each ultrasound beam, the receivers of the transducer, and the delay-and-sum beam-former, respectively. Specifically, after a focused ultrasound beam is transmitted as shown in Fig. 1(a), the ultrasound beam is reflected from some tissue boundaries and the reflected US data is recorded by Rx as RF data (see Fig. 1(b)). Thus, Depth-Rx coordinate RF data is obtained for each transmit event, and this is repeated to obtain a 3-D cube of RF data in the Depth-Rx- X_{mit} coordinates.

In practice, this B-mode acquisition is usually combined with multi-line acquisition (MLA) or parallel beam-forming (multiple parallel receive beams for each transmit beam) [41]–[43] to increase the frame rate. The concept is illustrated in Fig. 2, which shows the MLA procedure for four and eight parallel beams (denoted by 4MLA and 8MLA, respectively).

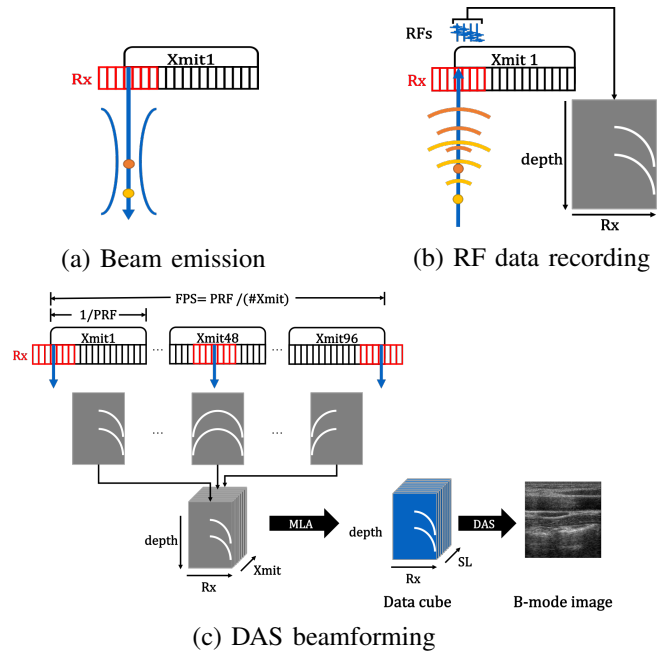


Fig. 1. Imaging flow of the standard B-mode ultrasound imaging. PRF : pulse repetition frequency, FPS : frame per second.

More specifically, for each transmit event, additional scan lines (SLs) are synthesized from the same Rx measurements using pre-defined offsets and weights [41]–[43]. This can increase the frame-rate thanks to fewer transmit events with the same number of scan lines.

Finally, a DAS beam-former uses the resulting Depth-Rx-SL data to generate an image frame (see Fig. 1(c)). Depending on the scanner, the DAS beam-former can be implemented using either hardware or software.

B. RF Sub-sampled MLA

Here, we consider two types of RF sub-sampling schemes. The first is a random Rx sub-sampling [34] that acquires only random subsets of Rx data for each transmit event. When combined with MLA, the same sub-sampled Rx data affect multiple parallel beams for each transmit event as shown in Figs. 3(a)(c). This sub-sampling scheme can be easily used to reduce data transmission bandwidth and power-consumption. However, it is usually associated with image artifacts and contrast loss. Second, we consider uniform sub-sampling of the X_{mit} event as shown in Figs. 3(b)(d) to further increase the frame rate. However, once a transmit event is skipped, all the associated SLs from the transmit event cannot be synthesized as shown in Figs. 3(b)(d). To retain the same number of scan lines, the number of parallel beams should be increased accordingly. However, use of the same Rx measurement to generate a large number of SLs introduces image artifacts and reduces the contrast.

III. MAIN CONTRIBUTION

Since these RF-subsampling schemes are usually associated with artifacts, in this section, a neural network is designed to achieve high quality reconstruction from the RF sub-sampling schemes.

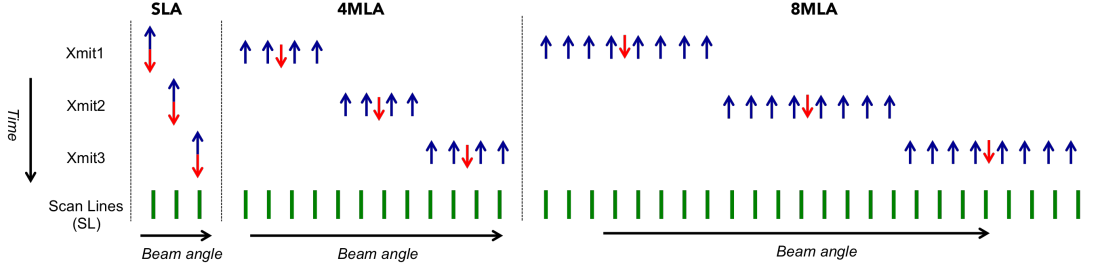


Fig. 2. Comparison of SLA, 4MLA, and 8MLA [41]. Down arrows indicate transmit directions and up arrows receive directions. For SLA, transmit and receive directions are identical. For MLA, different scan lines are generated by shifting Rx measurements. The synthesized scan line directions are indicated with lines at the bottom of the illustration.

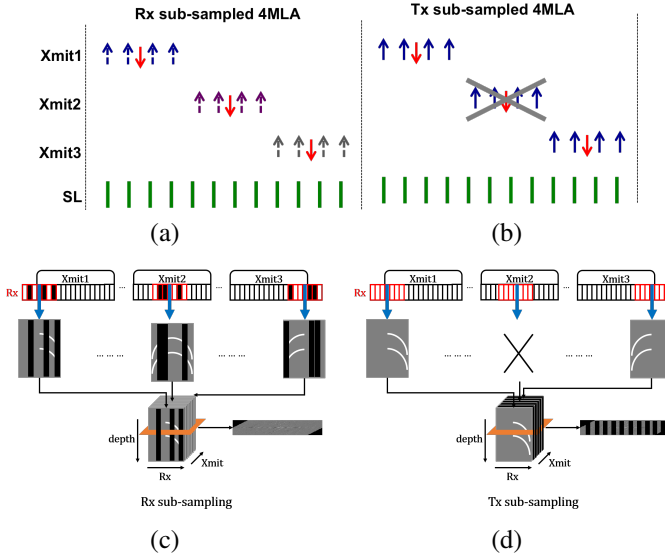


Fig. 3. RF subsampled MLA: (a)(c) Rx sub-sampled MLA and its acquisition example. Same color-coded dashed up arrows indicates the receiver direction that are affected from the same Rx subsampling. (b)(d) Tx sub-sampled MLA and its acquisition example. Once a transmit event is skipped, all the scan lines synthesized from the transmit cannot be generated. Down arrows indicate transmit directions and up arrows receive directions. The synthesized scan line directions are indicated with lines at the bottom of the illustration.

A. Redundancy of RF data and low-rank Hankel matrix

In B-mode ultrasound imaging, the direction of each transmit event changes incrementally, so the acquired Rx data does not change rapidly for each transmit event. This implies that some degree of skew redundancy exists in the Rx-Xmit (or Rx-SL) coordinate data and it can be easily seen as sparsity in the Fourier domain as demonstrated in Fig. 4.

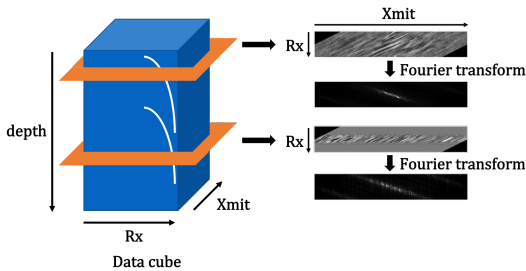


Fig. 4. Rx-Xmit data from depth-Rx-Xmit data cube and its Fourier spectrum.

Therefore, when the Fourier spectrum of the Rx-Xmit image

is denoted by $\widehat{F}(\omega)$, we can find a function $\widehat{K}(\omega)$ in the spectral domain such that their multiplication becomes zero [35]–[38]:

$$\widehat{F}(\omega)\widehat{K}(\omega) = 0, \quad \forall \omega. \quad (1)$$

This is equivalent to the convolutional relationship in the Rx-Xmit domain:

$$F \circledast K = 0, \quad (2)$$

where $F \in \mathbb{R}^{n_1 \times n_2}$ denotes the discrete 2-D image and $K \in \mathbb{R}^{d_1 \times d_2}$ is often referred to as the *annihilating filter* [11]. This can be represented in a matrix form:

$$\mathbb{H}_{d_1, d_2}(F) \overline{\text{VEC}}(K) = 0, \quad (3)$$

where $\text{VEC}(K)$ denotes the vectorization operation by stacking the column vectors of the 2-D matrix K , and $\overline{\text{VEC}}(K)$ is a flipped (i.e. index reversed) version of the vector $\text{VEC}(K)$. Here, $\mathbb{H}_{d_1, d_2}(F) \in \mathbb{R}^{n_1 n_2 \times d_1 d_2}$ is the *block Hankel matrix* for the image $F = [f_1, \dots, f_{n_2}] \in \mathbb{R}^{n_1 \times n_2}$, which is defined under the periodic boundary condition as follows [35]–[38]:

$$\mathbb{H}_{d_1, d_2}(F) = \begin{bmatrix} \mathbb{H}_{d_1}(f_1) & \mathbb{H}_{d_1}(f_2) & \cdots & \mathbb{H}_{d_1}(f_{d_2}) \\ \mathbb{H}_{d_1}(f_2) & \mathbb{H}_{d_1}(f_3) & \cdots & \mathbb{H}_{d_1}(f_{d_2+1}) \\ \vdots & \vdots & \ddots & \vdots \\ \mathbb{H}_{d_1}(f_{n_2}) & \mathbb{H}_{d_1}(f_1) & \cdots & \mathbb{H}_{d_1}(f_{d_2-1}) \end{bmatrix}, \quad (4)$$

and $\mathbb{H}_{d_1}(f_i) \in \mathbb{R}^{n_1 \times d_1}$ is a Hankel matrix:

$$\mathbb{H}_d(f_i) = \begin{bmatrix} f_i[1] & f_i[2] & \cdots & f_i[d_1] \\ f_i[2] & f_i[3] & \cdots & f_i[d_1 + 1] \\ \vdots & \vdots & \ddots & \vdots \\ f_i[n_1] & f_i[1] & \cdots & f_i[d_1 - 1] \end{bmatrix}. \quad (5)$$

Eq. (3) implies that the block Hankel matrix constructed from the RF data in the Rx-Xmit domain is rank-deficient. Furthermore, its rank is determined by the sparsity level in the spectral domain as theoretically proven in [38]. In fact, Jin *et al.* [34] utilized this to interpolate missing RF data using low-rank Hankel matrix completion by solving the following optimization problem:

$$(P) \quad \min_{M \in \mathbb{R}^{n_1 \times n_2}} \|F - M\|^2 \quad (6)$$

$$\text{subject to} \quad \text{RANK } \mathbb{H}_{d_1, d_2}(M) = s, \quad (7)$$

$$\mathcal{P}_\Lambda[F] = \mathcal{P}_\Lambda[M],$$

where Λ denotes the measured RF indices. This low-rank constraint optimization problem can be solved by matrix factorization [35]–[37], [44], [45]. However, the main limitation of [34] is its computational complexity (see Appendix A for the details). Moreover, [34] additionally requires exploitation of temporal domain redundancy, which often results in reduced temporal resolution.

B. RF Interpolation using Deep Learning

It was recently demonstrated in [40] that a *properly designed* deep neural network is the signal space manifestation of the factorization of a *high-dimensionally lifted* signal. Here, we briefly review the underlying idea.

Specifically, for a given signal $F \in \mathbb{R}^{n_1 \times n_2}$, consider its high dimensional *lifting* using a Hankel matrix $\mathbb{H}_{d_1, d_2}(F) \in \mathbb{R}^{n_1 n_2 \times d_1 d_2}$ in (4). Now, consider matrices $\Phi, \tilde{\Phi} \in \mathbb{R}^{n_1 n_2 \times m}$ which satisfy

$$\tilde{\Phi}\Phi^\top = \alpha I_{n_1 n_2}, \quad \alpha > 0, \quad (8)$$

where I_n denotes the $n \times n$ identity matrix. In [40], the matrices $\Phi, \tilde{\Phi}$ were identified as the pooling and unpooling, respectively. In addition, consider the additional set of matrices $\Psi, \tilde{\Psi} \in \mathbb{R}^{d_1 d_2 \times s}$ satisfying

$$\Psi\tilde{\Psi}^\top = P_{R(V)}, \quad (9)$$

where $P_{R(V)}$ denotes the projection matrix to the range space of V , and V is the basis vector for the row subspace of $\mathbb{H}_{d_1, d_2}(F)$. In [40], $\Psi, \tilde{\Psi}$ are identified as learnable convolution filters.

Using Eqs. (8) and (9), it is trivial to see that

$$\begin{aligned} \mathbb{H}_{d_1, d_2}(F) &= \frac{1}{\alpha} \tilde{\Phi}\Phi^\top \mathbb{H}_{d_1, d_2}(F) \Psi\tilde{\Psi}^\top, \\ &= \tilde{\Phi}C\tilde{\Psi}^\top, \end{aligned} \quad (10)$$

where the so-called convolution framelet coefficients are defined as

$$C := \frac{1}{\alpha} \Phi^\top \mathbb{H}_{d_1, d_2}(F) \Psi. \quad (11)$$

Thanks to the property of the Hankel matrix, (11) can be equivalently represented using the convolution [40]:

$$C = \Phi^\top (F \circledast H), \quad (12)$$

where the multi-channel filter $H := H(\Psi/\alpha)$ can be obtained by arranging the elements of Ψ after scaling by $1/\alpha$. Next, the high dimensional representation (10) can be *unlifted* to the original signal space as follows [40]:

$$F = (\tilde{\Phi}C) \circledast G, \quad (13)$$

where the multi-channel filter $G := G(\tilde{\Psi})$ can be obtained by rearranging the elements of $\tilde{\Psi}$.

It is important to note that the convolutions in (12) and (13) are exactly the same convolutions used for the existing convolutional neural network [40]. In fact, the structure in (12) and (13) corresponds to the popular encoder-decoder network architecture, where the number of filter channels is determined by the number of columns of Ψ and $\tilde{\Psi}$. This confirms that an

encoder-decoder network can be derived as the signal space manifestation of the Hankel matrix decomposition in a high-dimensional space.

Based on these findings, it is easy to see that a feasible solution for (P) satisfies the encoder-decoder network structure:

$$M = (\tilde{\Phi}C) \circledast G, \quad C := \Phi^\top (M \circledast H),$$

where the number of channels for the filters H and G is s . The authors in [40] found that although the pooling and unpooling operations Φ and $\tilde{\Phi}$ can be pre-defined based on domain knowledge, the filters should be learned from the training data. Then, for a given set of sub-sampled RF data $Y^{(i)} := P_\Lambda [F^{(i)}]$ and fully sampled data $F^{(i)}$ for $i = 1, \dots, n_t$, the filter learning problem can be readily obtained from (P) as follows:

$$\min_{H, G} \sum_{i=1}^{n_t} \left\| F^{(i)} - \mathcal{K} \left(Y^{(i)}; H, G \right) \right\|^2, \quad (14)$$

where the operator $\mathcal{K} : \mathbb{R}^{n_1 \times n_2} \rightarrow \mathbb{R}^{n_1 \times n_2}$ is defined as

$$\mathcal{K} \left(Y^{(i)}; H, G \right) = (\tilde{\Phi}C(Y^{(i)})) \circledast G,$$

in terms of the mapping $C : \mathbb{R}^{n_1 \times n_2} \rightarrow \mathbb{R}^{n_1 \times n_2}$

$$C(Y) = \Phi^\top (M \circledast H), \quad \forall Y \in \mathbb{R}^{n_1 \times n_2}.$$

At the inference stage, the interpolated RF data can be readily obtained from the sub-sampled RF data \tilde{Y} using the learned filters:

$$\tilde{F} = \mathcal{K} \left(\tilde{Y}; H, G \right).$$

The filter learning problem in (14) can be easily extended for an encoder-decoder network with ReLU [40], [46]. The role of the rectified linear unit (ReLU) then guides the learning procedure such that the output signal can be represented as the nonnegative (conic) combination of the learned convolution framelet basis [46]. This so-called *conic coding* is popular for learning part-by-part representations of objects [47], [48], which constitute the key ingredients of nonnegative matrix factorization (NMF) [48], [49].

Simple signal expansion using (12) and (13) with ReLU is so powerful that a deep encoder-decoder neural network architecture emerges from recursive application of this convolutional framelet expansion with ReLU to the framelet coefficients (11). The cascaded encoder-decoder network with ReLU results in an exponentially increasing expressiveness [31] that can capture US specific image features that would not have been possible with ALOHA. This is the primary motivation for our interest in using a deep neural network as a generalization beyond the low-rank Hankel matrix approach.

Finally, a *properly designed* network refers to a network that satisfies the condition (8), which is often called the frame condition [40]. For example, the following two sets of pooling and unpooling operations satisfy the frame condition (8):

$$\Phi_1 = \tilde{\Phi}_1 = I_{n_1 n_2}, \quad \Phi_2 = \tilde{\Phi}_2 = \begin{bmatrix} I_{n_1 n_2} & I_{n_1 n_2} \end{bmatrix} \quad (15)$$

Here, the first set of basis $(\Phi_1, \tilde{\Phi}_1)$ constitute a complete basis, whereas the second set of basis is redundant. The corresponding multi-layer encoder-decoder network structures

are illustrated in Figs. 5(a) and (b), respectively. Note that redundancies in the pooling/unpooling layers in $\Phi_2, \tilde{\Phi}_2$ are recognized as skipped connections. In general, depending on the choice of pooling and unpooling matrices, various network forms can be derived. See [25] for more details.

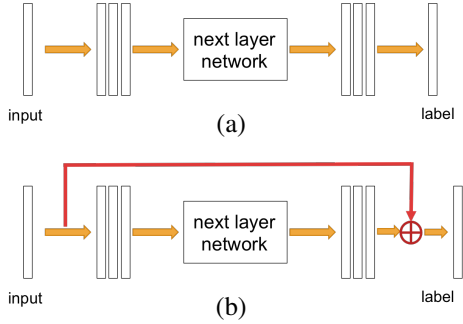


Fig. 5. Deep convolutional framelet architecture with (a) $\Phi_1, \tilde{\Phi}_1$ and (b) $\Phi_2, \tilde{\Phi}_2$ in Eq. (15). Here, each bar represents a channel so that the number of channels is $s = 3$ at the first layer decomposition. Similar encoder-decoder network are recursively applied to the three-channel feature map.

In short, because of the redundancy in the Rx-Xmit (or Rx-SL) domain data, the associated Hankel matrix is low-ranked, which allows a direct interpolation of the Rx-Xmit (or Rx-SL) domain RF data using deep CNN. Moreover, thanks to the nonlinearity and cascaded implementation, a properly designed neural network has exponentially increasing expressiveness suitable for interpolating diverse RF data.

IV. METHOD

A. Data set

For experimental verification, multiple RF data were acquired with the E-CUBE 12R US system (Alpinion Co., Korea). For data acquisition, we used a linear array transducer (L3-12H) with a center frequency of 8.48 MHz and a convex array transducer (SC1-4H) with a center frequency of 3.2 MHz. The configuration of the probes is given in Table I.

TABLE I
PROBES CONFIGURATION

Parameter	Linear Probe	Convex Probe
Probe Model No.	L3-12H	SC1-4H
Carrier wave frequency	8.48 MHz	3.2 MHz
Sampling frequency	40 MHz	40 MHz
No. of probe elements	192	192
No. of Tx elements	128	128
No. of Xmit events	96	96
No. of Rx elements	64	64
Elements pitch	0.2 mm	0.348 mm
Elements width	0.14 mm	0.26 mm
Elevating length	4.5 mm	13.5 mm
Parallel beamforming	4MLA	4MLA

Using a linear probe, we acquired RF data from the carotid area from 10 volunteers. The data consisted of 40 temporal frames per subject, providing 400 sets of Depth-Rx-Xmit data cube. The dimension of each Rx-Xmit plane was 64×96 . A set of 30,000 Rx-Xmit planes was randomly selected from the 400 sets of data cubes, then divided into 25,000 datasets

for training and 5000 datasets for validation. The remaining dataset of 360 frames was used as a test dataset.

In addition, we acquired 100 frames of RF data from the abdominal regions of two subjects using a convex array transducer. The size of each Rx-Xmit plane in the convex probe case was also 64×96 . This dataset was only used for test purposes and no additional training of CNN was performed on it. The convex dataset was used to verify the generalization power of the proposed algorithm.

In both probes, the default setup for parallel beam formation was 4MLA, i.e., for each transmit event, four scan lines were synthesized.

B. RF Sub-sampling Scheme

For Rx sub-sampling experiments, the Rx data for each transmit event were randomly sub-sampled at a down-sampling factor of $\times 4$ or $\times 8$. Since the receiver at the center gets the RF data from direct reflection as shown in Fig. 1(c), the RF data from the center of the active receivers set were always included to improve the performance.

We also considered sub-sampling in both the Xmit event and Rx direction. Specifically, the RF data was uniformly sub-sampled along the transmit event with a down-sampling factor of $\times 2$, which is followed by random subsampling along the Rx direction at a down-sampling ratio of 4 for each transmit event. This scheme can potentially increase the number of temporal frames twice, and reduce the Rx power consumption by 4.

C. Network Architecture

For the Rx sub-sampling scheme, CNN was applied to 64×96 data in the Rx-Xmit plane. The interpolated data was later expanded to the 64×384 Rx-SL plane using the parallel beam-forming scheme as shown in Fig. 6(a). For Rx-Xmit sub-sampling, due to the uniform subsampling artifacts, the following scheme was found to be better. Specifically, the RF data was first expanded into the 64×384 Rx-SL plane using 8MLA. CNN was then applied to the 64×384 Rx-SL plane as shown in Fig. 6(b).

The proposed CNN is composed of convolution layers, batch normalization layers, ReLU layers and a contracting path with concatenation as shown in Figs. 6(a) and (b). Specifically, the network consists of 28 convolution layers composed of a batch normalization and ReLU except for the last convolution layer. The first 27 convolution layers use 3×3 convolutional filters (i.e. the 2-D filter has a dimension of 3×3), and the last convolution layer uses a 1×1 filter. Four contracting paths with concatenation exist. If the sub-sampling ratio is greater than 4, an additional convolutional layer with a 3×3 filter, batch normalization layer, and ReLU layer is inserted in each module to enlarge the receptive field size. Note that the proposed architecture is a combination of two basic architectures in Figs. 5(a) and (b).

The network was implemented with both TensorFlow [50] and MatConvNet [51] in the MATLAB 2015b environment to verify the platform-dependent sensitivity. We found that with the same training strategy, the two implementations provided near identical results. Specifically, for network training, the

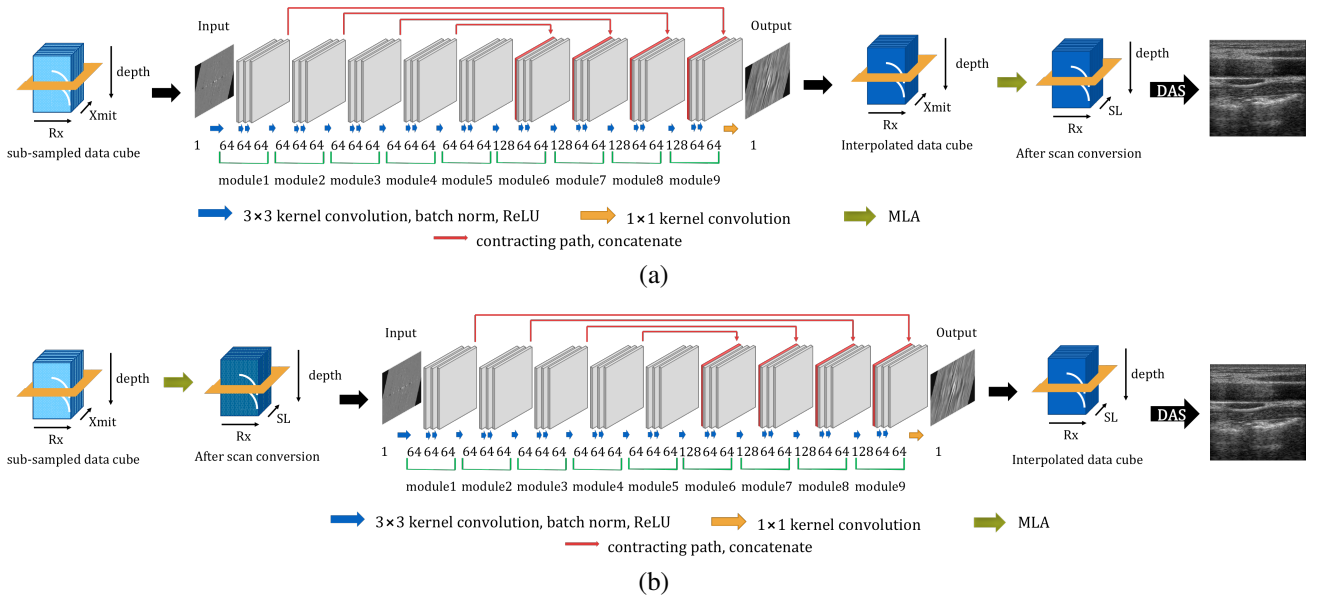


Fig. 6. Our network architecture for RF-interpolation for (a) Rx sub-sampling, and (b) Rx-Xmit sub-sampling.

parameters were estimated by minimizing the l_2 norm loss function. The network was trained using a stochastic gradient descent with a regularization parameter of 10^{-4} . The learning rate started from 10^{-7} and gradually decreased to 10^{-9} . The weights were initialized using Gaussian random distribution with the Xavier method [52]. The number of epochs was 500 for all down-sampling rates. To avoid over-fitting during Rx-Xmit sub-sampling, the neural network was first trained with 4x Rx down-sampled data, and after 200 epochs, the network was fine-tuned for expanded Rx-Xmit sub-sampled data.

The network was trained for random down sampling patterns to avoid bias to specific to sampling patterns. However, for each down-sampling scheme (e.g. x4, x8 and 4x2), a separate CNN was trained.

D. Baseline algorithms

For comparative studies, our CNN based interpolation was first compared with the linear interpolation results. Specifically, due to the irregular down-sampling pattern, the standard linear interpolation algorithm did not work, so we used the grid-based 3D interpolation function `griddata()` in MATLAB. However, at high sub-sampling ratios, the Rx-Xmit plane interpolation using `griddata()` still resulted in significant artifacts, so we used multiple temporal frames together for 3-D interpolation to improve the performance.

We also compared the annihilating filter-based low rank Hankel matrix approach (ALOHA) for RF interpolation [34], which also harnessed the correlation in the temporal direction in addition to the Rx-Xmit (or Rx-SL) domain redundancy. Specifically, due to correlation in the temporal direction, the RF data from adjacent temporal frames showed some level of redundancy, which could be exploited by ALOHA [35]. More specifically, we could find the multi-frame annihilating filter relationship [34]:

$$F_i \otimes K_j - F_j \otimes K_i = 0, \quad i \neq j, \quad (16)$$

where F_i denotes the RF data in the Rx-Xmit data at the i -th frame, and K_i are associated filters. Then, (16) can be represented in a matrix form:

$$\begin{bmatrix} \mathbb{H}_{d_1, d_2}(F_i) & \mathbb{H}_{d_1, d_2}(F_j) \end{bmatrix} \begin{bmatrix} \text{VEC}(K_i) \\ -\text{VEC}(K_j) \end{bmatrix} = 0 \quad (17)$$

so that the extended Hankel matrix $\begin{bmatrix} \mathbb{H}_{d_1, d_2}(F_i) & \mathbb{H}_{d_1, d_2}(F_j) \end{bmatrix}$ is rank-deficient. Similarly, we could construct an extended Hankel matrix using RF data from N -time frames:

$$\mathbb{H}_{d_1, d_2 | N}(\{F_i\}_{i=1}^N) := \begin{bmatrix} \mathbb{H}_{d_1, d_2}(F_1) & \cdots & \mathbb{H}_{d_1, d_2}(F_N) \end{bmatrix},$$

Due to the spatio-temporal correlation, the extended Hankel matrix still had a low rank [34]. Accordingly, the RF interpolation problem could be solved using the following low-rank Hankel matrix completion problem [34]:

$$\begin{aligned} \min_{\{M_i\}_{i=1}^N} & \quad \|\mathbb{H}_{d_1, d_2 | N}(\{M_i\}_{i=1}^N)\|_* \\ \text{subject to} & \quad P_\Lambda[F_i] = P_\Lambda[M_i], \quad i = 1, \dots, N, \end{aligned} \quad (18)$$

where Λ denotes the indices of the measured RF data and P_Λ denotes the projection to the index Λ . The optimization problem (18) can be solved using an alternating direction method of multiplier (ADMM) after matrix factorization [34].

The computational complexity of ALOHA is mainly determined by the number of annihilating filter sizes and the temporal frames. In our case, we used 10 temporal frames and an annihilating filter size of 7×7 . The rigorous complexity analysis of ALOHA is provided in Appendix A.

E. Performance Metrics

To quantitatively show the advantages of the proposed deep learning method, we used the contrast-to-noise ratio (CNR) [53], peak-signal-to-noise ratio (PSNR), structure similarity (SSIM) [54] and the reconstruction time.

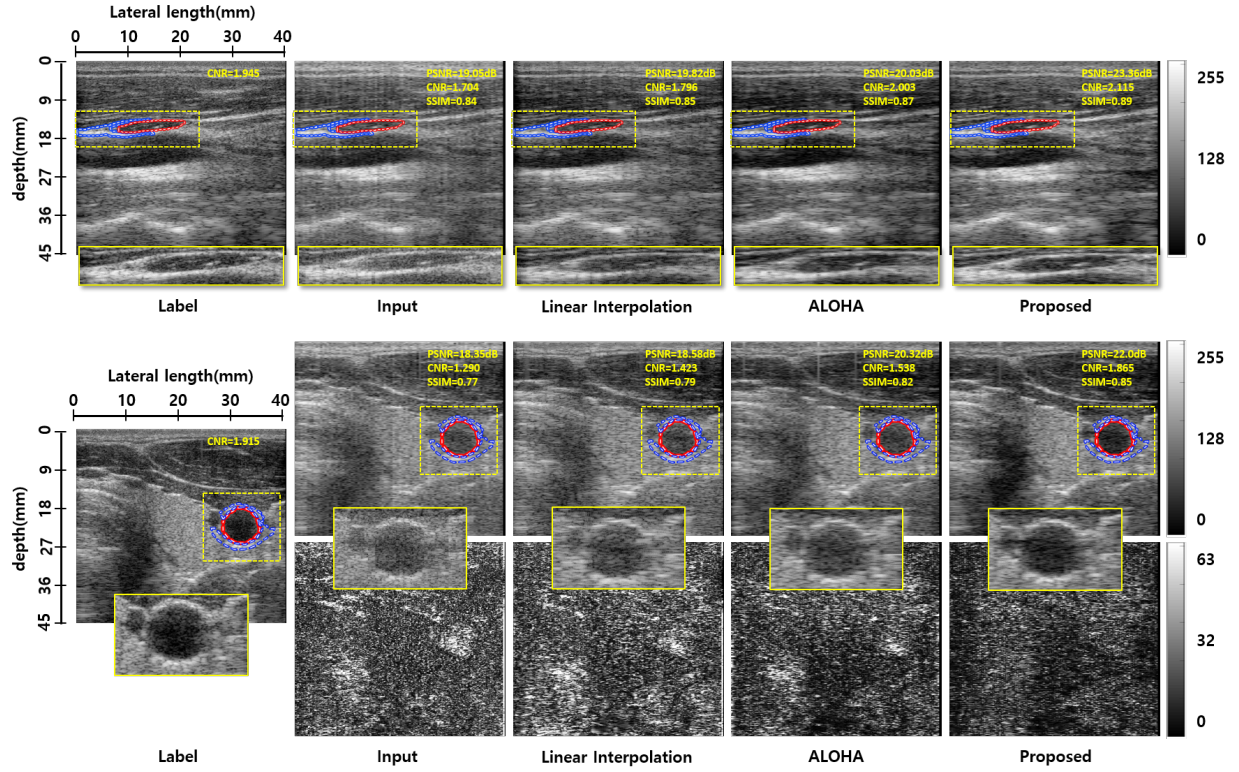
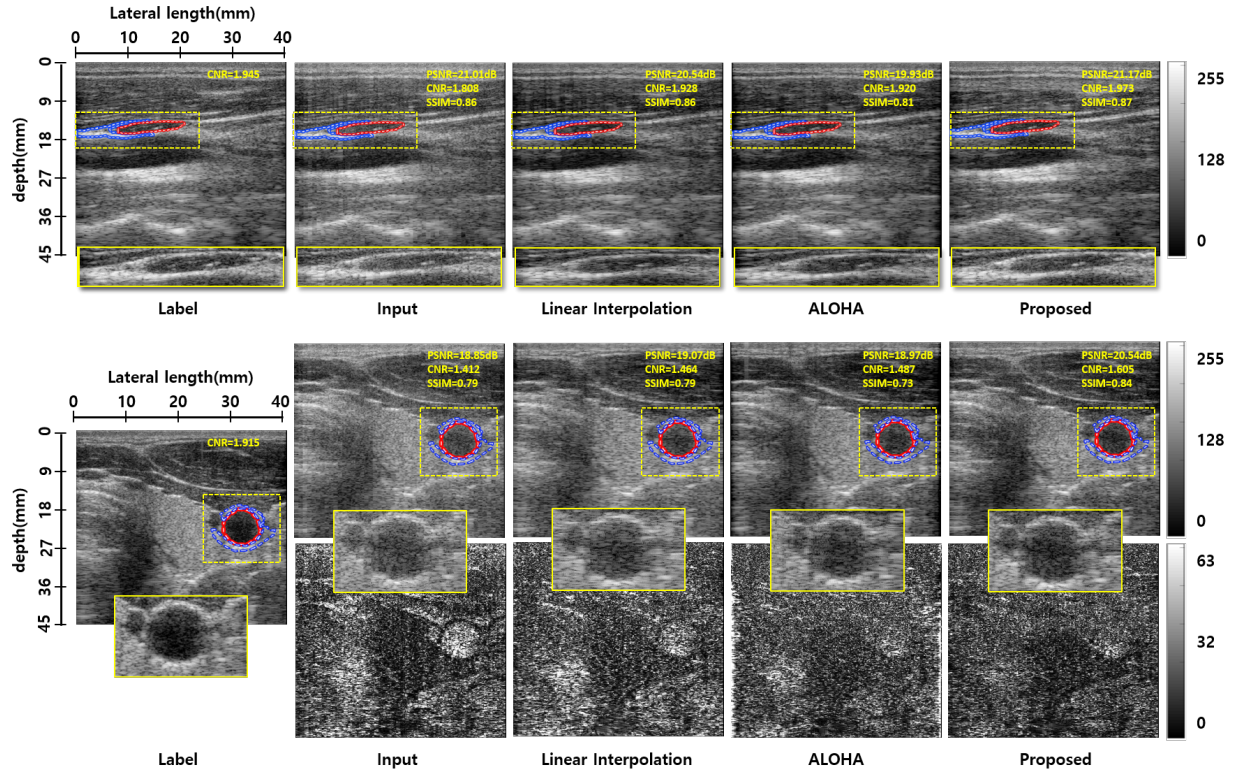
(a) $\times 8$ Rx sub-sampling results(b) 4×2 Rx-Xmit sub-sampling results

Fig. 7. Reconstruction results of linear array transducer DAS beamformer B-mode images of carotid region from two sets of sub-sampled RF data.

The CNR is measured for the background (B) and anechoic structure (aS) in the image, and is quantified as

$$\text{CNR}(B, aS) = \frac{|\mu_B - \mu_{aS}|}{\sqrt{\sigma_B^2 + \sigma_{aS}^2}}, \quad (19)$$

where μ_B , μ_{aS} , and σ_B , σ_{aS} are the local means, and the standard deviations of the background (B) and anechoic structure (aS) [53].

The PSNR and SSIM index are calculated on label (F) and reconstruction (\tilde{F}) images of common size $n_1 \times n_2$ as

$$\text{PSNR}(F, \tilde{F}) = 10 \log_{10} \left(\frac{n_1 n_2 R_{\max}^2}{\|F - \tilde{F}\|_F^2} \right), \quad (20)$$

where $\|\cdot\|_F$ denotes the Frobenius norm and $R_{\max} = 2^{(\#bits \text{ per pixel})} - 1$ is the dynamic range of pixel values (in our experiments this is equal to 255), and

$$\text{SSIM}(F, \tilde{F}) = \frac{(2\mu_F \mu_{\tilde{F}} + c_1)(2\sigma_{F, \tilde{F}} + c_2)}{(\mu_F^2 + \mu_{\tilde{F}}^2 + c_1)(\sigma_F^2 + \sigma_{\tilde{F}}^2 + c_2)}, \quad (21)$$

where μ_F , $\mu_{\tilde{F}}$, σ_F , $\sigma_{\tilde{F}}$, and $\sigma_{F, \tilde{F}}$ are the local means, standard deviations, and cross-covariance for images F and \tilde{F} calculated for a radius of 50 units. The default values of $c_1 = (k_1 R_{\max})^2$, $c_2 = (k_2 R_{\max})^2$, $k_1 = 0.01$ and $k_2 = 0.03$.

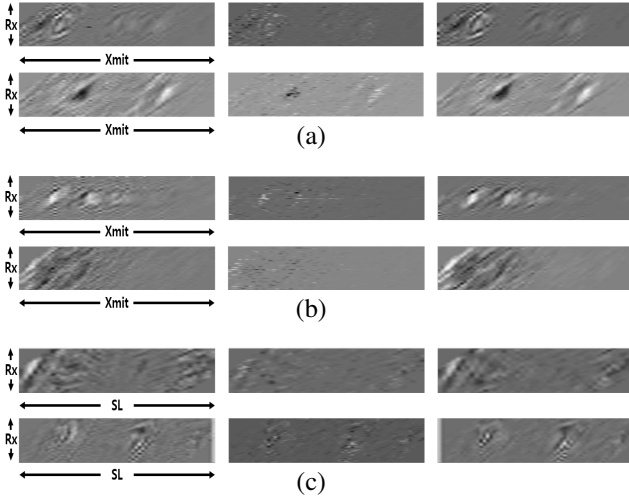


Fig. 8. Rx-SL coordinate RF data for (a) $\times 4$ Rx down-sampling, (b) $\times 8$ Rx down-sampling, (c) 2×4 Rx-Xmit down-sampling. Label denotes the fully sampled RF data, and output refers to the interpolated output from input using the proposed method.

V. EXPERIMENTAL RESULTS

A. Linear Array Transducer Experiments

Fig. 7 show the DAS beam-former output images for $8 \times$ Rx and 4×2 Rx-Xmit down-sampling schemes. Our method significantly improves the visual quality of the input image and outperforms other methods by eliminating line and block artifacts. From difference images in Fig. 7, it is evident that under both down-sampling schemes, the proposed method approximate both the near and the far field Rx-Xmit planes with equal efficacy and only few structural details are discernible. On the other hand, linear interpolation exhibits horizontal blur artifacts especially at the far field region as shown in the difference images.

Fig. 8 illustrates representative examples of Rx-SL coordinate data from the linear transducer for three different RF

down-sampling schemes. The proposed CNN-based interpolation successfully reconstructs the missing RF data in all down-sampling schemes. CNN automatically identifies the missing RF data and approximates it with available neighboring information. It is noteworthy that in the down-sampling schemes, the proposed method can efficaciously interpolates the missing data from as little as only 12.5% RF-data.

We compared the CNR, PSNR, and SSIM distributions of reconstructed B-mode images obtained from 360 test frames of a linear array. In Fig. 9(a), compared to the linear interpolation and ALOHA, the proposed method achieved average CNR values of 2.20, 2.19, and 1.85 in $\times 4$ Rx, $\times 8$ Rx and 4×2 Rx-Xmit sampling schemes, respectively. These values are 25.00%, 31.93% and 6.94% higher than the input, 17.65%, 21.67% and 1.65% higher than the linear interpolation results, and 14.58%, 19.02% and 12.12% higher than the ALOHA results.

Fig. 9(b) compares the PSNR distribution in $4 \times$ Rx, $8 \times$ Rx, and 4×2 Rx-Xmit sub-sampling schemes. Compared to linear interpolation, the proposed deep learning method showed 4.26dB, 3.64dB, and 1.44dB improvement on average for $4 \times$ Rx, $8 \times$ Rx, and 4×2 Rx-Xmit sub-sampling schemes, respectively. In comparison to ALOHA, the proposed deep learning method showed 1.76dB, 1.7dB, and 1.38dB improvement on average for $4 \times$ Rx, $8 \times$ Rx, and 4×2 Rx-Xmit sub-sampling schemes, respectively.

Unlike linear interpolation and ALOHA, which rely on temporal correlation of the RF data in multiple frames, the proposed method reconstructs each frame individually. Therefore, the structure similarity (SSIM) of the DAS beam-former images in the proposed algorithm is significantly high. Fig. 9(c) compare the SSIM in $4 \times$ Rx, $8 \times$ Rx, and 4×2 Rx-Xmit sub-sampling schemes. Compared to linear interpolation, the proposed deep learning method showed 19.44%, 21.21%, and 7.25% improvement in $4 \times$ Rx, $8 \times$ Rx, and 4×2 Rx-Xmit sub-sampling schemes, respectively. In comparison to ALOHA, the proposed deep learning method showed 6.17%, 8.11%, and 17.46% improvement in $4 \times$ Rx, $8 \times$ Rx, and 4×2 Rx-Xmit sub-sampling schemes, respectively.

Another important advantage of the proposed method is the run-time complexity. Although training required 96 hours for 500 epochs using Tensorflow, once training was completed, the reconstruction time for the proposed deep learning method was several orders of magnitude faster than those for ALOHA and linear interpolation (see Table II).

TABLE II
AVERAGE RECONSTRUCTION TIME (MILLISECONDS) FOR EACH RX-XMIT PLANES

Sub-sampling scheme	griddata()	ALOHA	Proposed
$\times 4$ Rx	41.0	65.5	1.0
$\times 8$ Rx	31.1	58.9	9.8
4×2 Rx-Xmit	38.2	107.0	1.0

B. Convex Array Transducer Experiments

The trained CNN from the linear array transducer was applied to the circular array transducer. Fig. 10 shows the

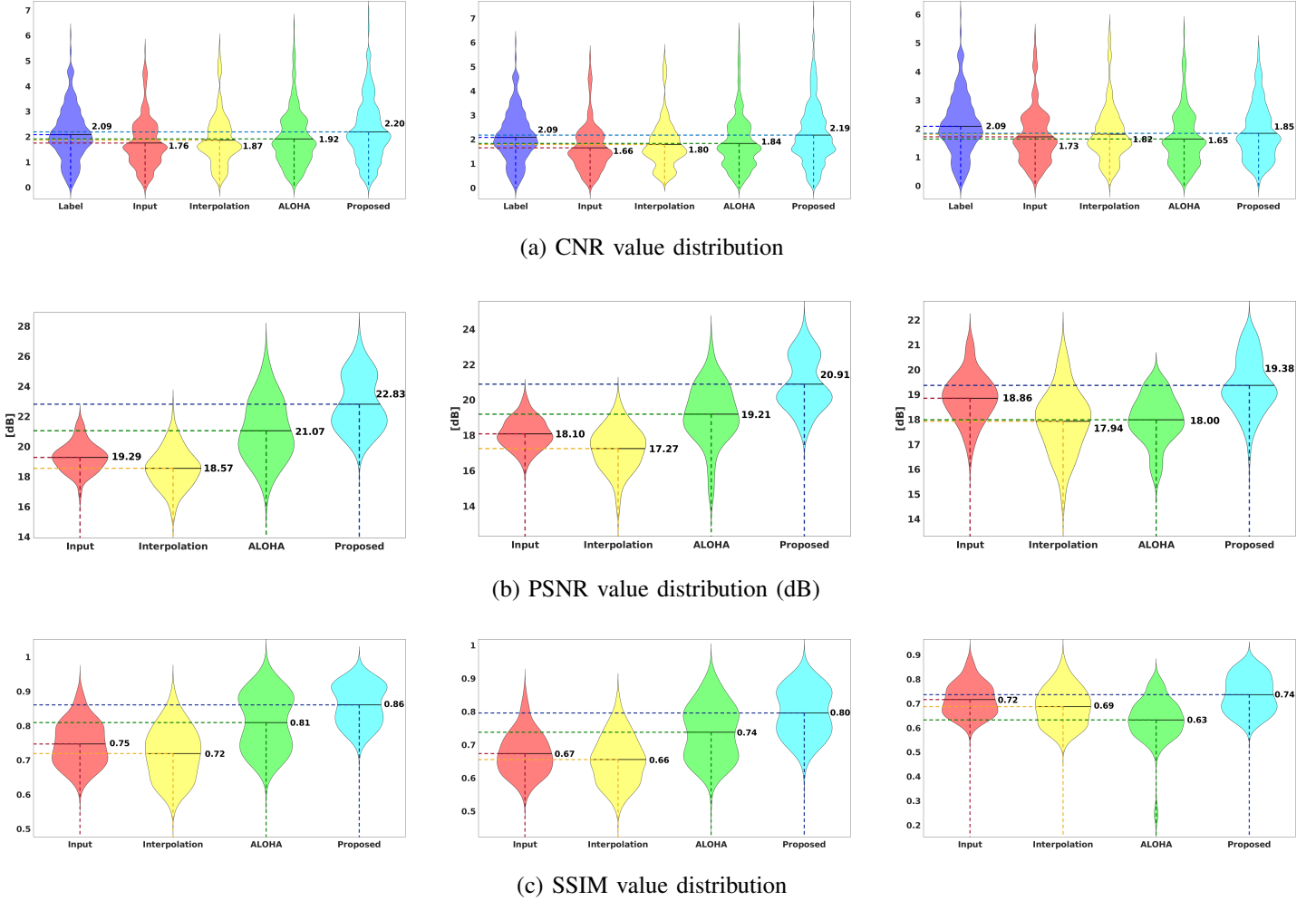


Fig. 9. Carotid region linear probe B-mode Reconstruction CNR, SSIM and PSNR value distribution of 360 images from various RF sub-sampling scheme: (First column) $4 \times$ Rx sub-sampling, (middle column) $8 \times$ Rx sub-sampling, (last column) 4×2 Rx-Xmit sub-sampling.

RF interpolated DAS beam-former output images for $8 \times$ Rx and 4×2 Rx-Xmit down-sampling schemes. Excellent image quality was obtained with the proposed method, which outperformed the existing algorithms. Moreover, many artifacts shown in the zoomed part of input images were successfully removed. Although the network was trained using linear array transducers, the performance improvement using the proposed algorithm in convex array transducer was similar to that for the linear array experiment.

We compared the CNR, PSNR, and SSIM distributions for reconstructed B-mode images obtained from 100 test frames of a convex array. As shown in Fig. 11(a), compared to the linear interpolation and ALOHA based interpolation, the proposed method achieved CNR values of 1.75, 1.70 and 1.49 in $4 \times$ Rx, $8 \times$ Rx and 4×2 Rx-Xmit sampling schemes, respectively. These values are 24.11%, 23.19% and 4.20% higher than those for sub-sampled input, 19.05%, 25.93% and 7.19% higher than those for linear interpolation, and 12.18%, 15.65% and 14.62% higher than those for ALOHA.

In this experiment, the quantitative improvement of contrast was high as in the linear array cases, and it is remarkable that accurate reconstruction was still obtained for the abdominal

region, which was never observed with the network trained using the linear array transducer data. The results confirmed the generalization power of the algorithm.

Fig. 11(b) compares the PSNR distribution in $4 \times$ Rx, $8 \times$ Rx, and 4×2 Rx-Xmit sub-sampling schemes. Compared to linear interpolation, the proposed deep learning method showed 3.22dB, 2.69dB, and 1.26dB improvement on average for $4 \times$ Rx, $8 \times$ Rx, and 4×2 Rx-Xmit sub-sampling schemes, respectively. In comparison to ALOHA, the proposed deep learning method showed 0.98dB, 1.09dB, and 1.05dB improvement on average for $4 \times$ Rx, $8 \times$ Rx, and 4×2 Rx-Xmit sub-sampling schemes, respectively.

In the convex array, the structural similarity (SSIM) of the DAS beam-former images in the proposed algorithm was higher than that obtained with contemporary methods. Fig. 11(c) compares the SSIM in $4 \times$ Rx, $8 \times$ Rx, and 4×2 Rx-Xmit sub-sampling schemes. Compared to linear interpolation, the proposed deep learning method showed 9.76%, 8.97%, and 3.75% improvement in $4 \times$ Rx, $8 \times$ Rx, and 4×2 Rx-Xmit sub-sampling schemes, respectively. In comparison to ALOHA, the proposed deep learning method showed 4.65%, 4.94%, and 1.22% improvement in $4 \times$ Rx, $8 \times$ Rx, and 4×2

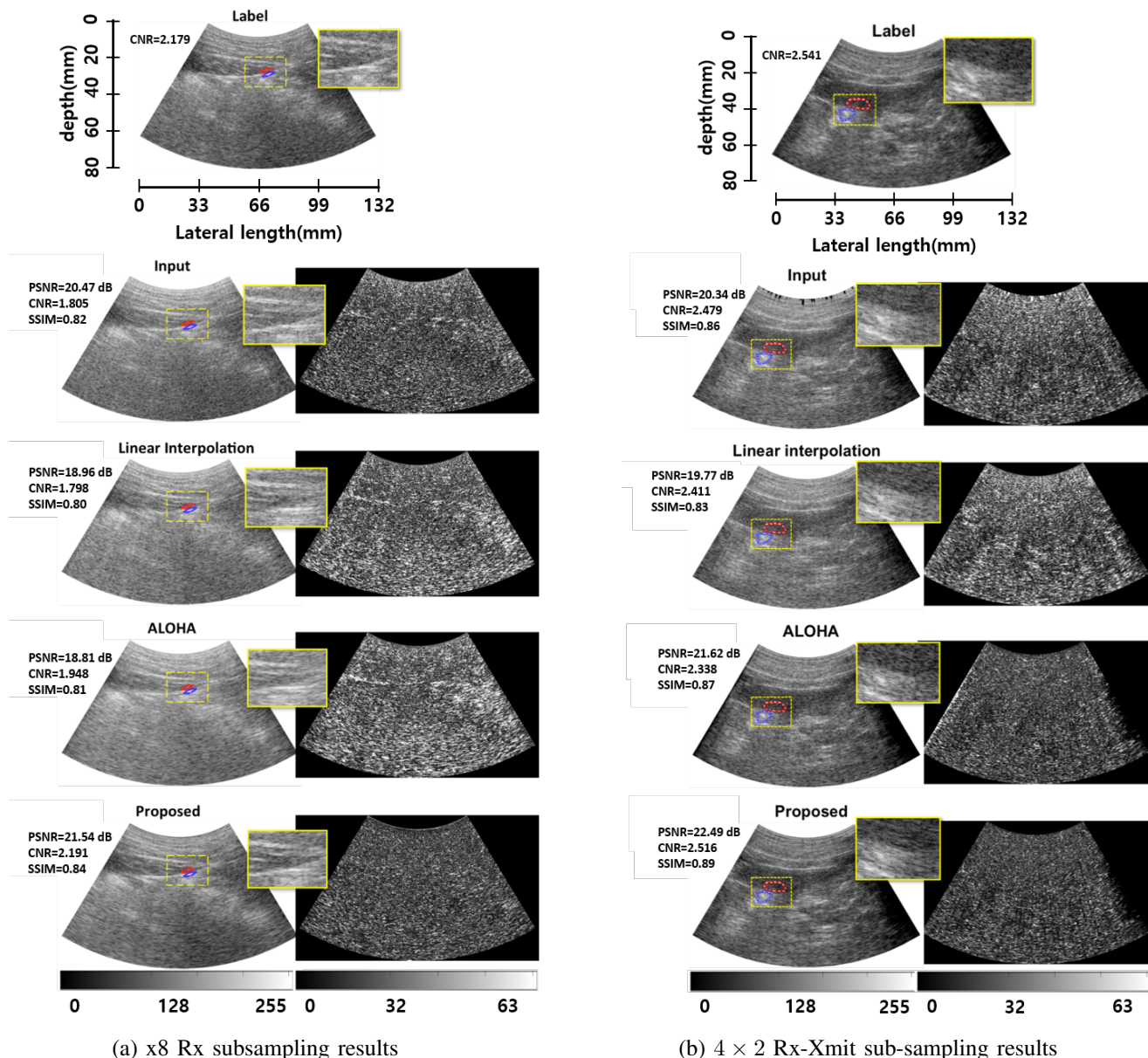


Fig. 10. Reconstruction results for abdominal region (liver) from sub-sampled RF data using the convex probe.

Rx-Xmit sub-sampling schemes, respectively.

VI. CONCLUSIONS

In this paper, we presented a novel deep learning approach for accelerated B-mode ultrasound imaging. Inspired by the recent discovery of a close link between deep neural network and Hankel matrix decomposition, we searched for a signal domain in which the Hankel structured matrix is sufficiently low-ranked. Our analysis showed that there are significant redundancies in the Rx-Xmit and Rx-SL domains, which results in a low-rank Hankel matrix. Thus, to exploit the redundancy in the RF domain, the proposed CNN was applied to the Rx-Xmit or Rx-SL domains. In contrast to existing CS approaches that require hardware changes or computationally expensive algorithms, the proposed method does not require any hardware change and can be applied to any B-mode

ultrasound system or transducer. Moreover, thanks to the exponentially increasing expressiveness of deep networks, PSNR, SSIM, and CNR were significantly improved over ALOHA and other existing methods, and the run-time complexity was orders of magnitude faster. Therefore, this method can be an important platform for RF sub-sampled US imaging.

VII. ACKNOWLEDGEMENT

This work was supported by the National Research Foundation of Korea, Grant number NRF-2016R1A2B3008104.

APPENDIX A: COMPLEXITY ANALYSIS

According to the analysis in [35], the complexity of ALOHA is mainly determined by matrix inversion during the ADMM step. For a given $n_1 \times n_2$ RF data, in our ALOHA

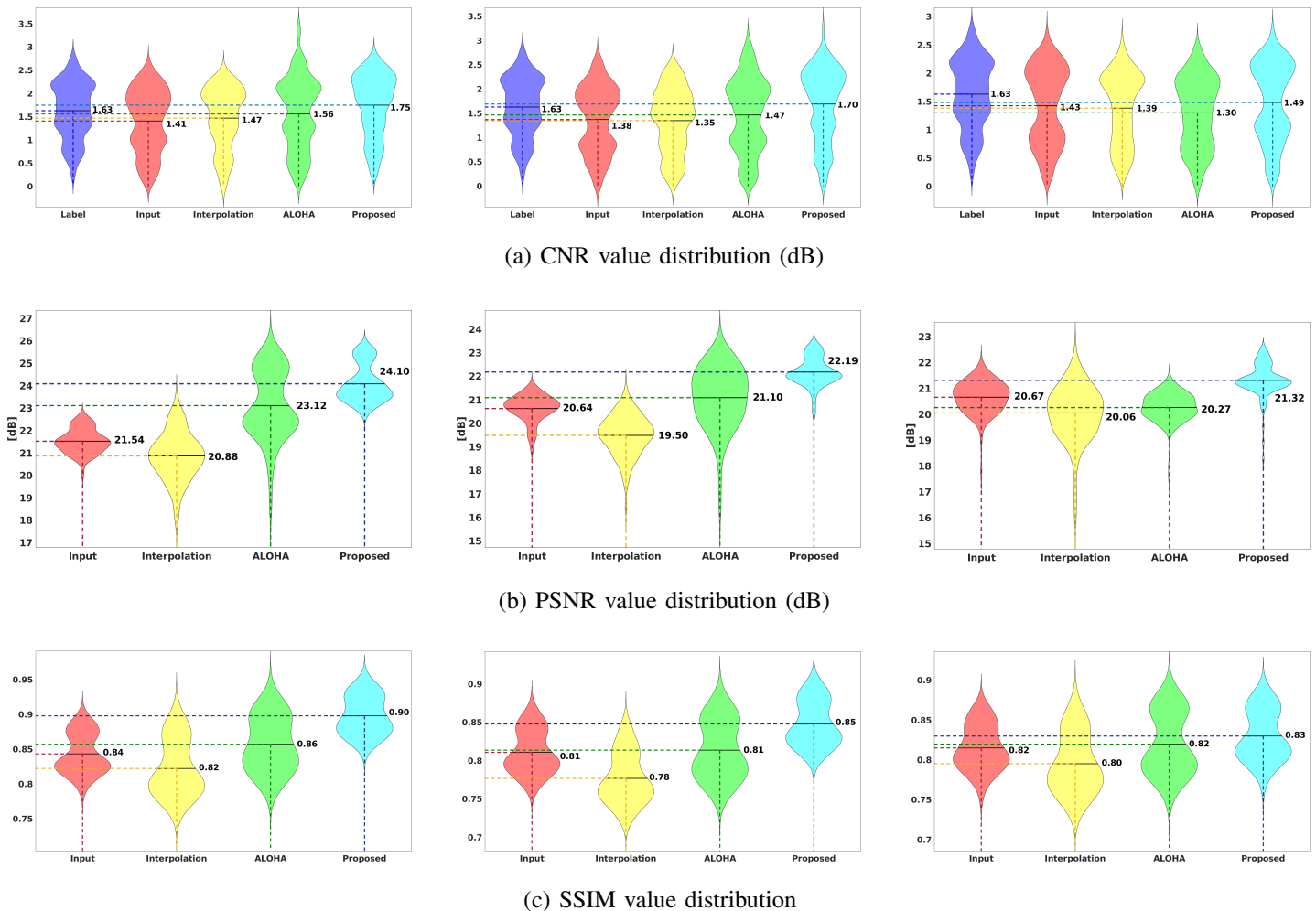


Fig. 11. Abdominal region convex probe B-mode Reconstruction CNR, PSNR and SSIM value distribution of 100 images from various RF sub-sampling scheme: (First column) $x4$ Rx sub-sampling, (middle column) $x8$ Rx sub-sampling, (last column) $4x2$ Rx-Xmit sub-sampling.

implementation, the annihilating filter size was $d_1 \times d_2 = 7 \times 7$, and the number of adjacent frames was $N = 10$. Thus, the computational complexity for each matrix inversion is given by $\mathcal{O}(n_1 n_2 (d_1 d_2 N)^2 + (d_1 d_2 N)^3)$ per iteration, which is equal to $\mathcal{O}(n_1 n_2 470^2 + 470^3)$, where \mathcal{O} denotes the “big O” notation. Furthermore, there are two matrix inversions for each ADMM step and at least 50 iterations were required for convergence.

On the other hand, in our CNN implementation, we used $d \times d = 3 \times 3$ filters and the number of channels was $K = 64$. Since there exist no matrix inversions and all the operations were by convolutions, the computational complexity for each multi-channel convolution layer with 64 input and 64 output channels is given by $\mathcal{O}(n_1 n_2 (dK)^2) = \mathcal{O}(n_1 n_2 192^2)$. In addition, the number of convolutional layers was 28. Thus, the overall computational complexity of CNN is lower than that of ALOHA.

REFERENCES

- [1] Y. H. Yoon and J. C. Ye, “Deep learning for accelerated ultrasound imaging,” in *2018 IEEE International Conference on Conference on Acoustics, Speech and Signal Processing (ICASSP)*, also available as *arXiv preprint arXiv:1710.10006*. IEEE, 2018.
- [2] B. P. Nelson and K. Chason, “Use of ultrasound by emergency medical services: a review,” *International journal of emergency medicine*, vol. 1, no. 4, pp. 253–259, 2008.
- [3] G. R. Lockwood, J. R. Talman, and S. S. Brunke, “Real-time 3-D ultrasound imaging using sparse synthetic aperture beamforming,” *IEEE Trans. Ultrason., Ferroelect., Freq. Control*, vol. 45, no. 4, pp. 980–988, 1998.
- [4] E. Macé, G. Montaldo, I. Cohen, M. Baulac, M. Fink, and M. Tanter, “Functional ultrasound imaging of the brain,” *Nature methods*, vol. 8, no. 8, pp. 662–664, 2011.
- [5] M. Tanter and M. Fink, “Ultrafast imaging in biomedical ultrasound,” *IEEE transactions on ultrasonics, ferroelectrics, and frequency control*, vol. 61, no. 1, pp. 102–119, 2014.
- [6] H. Liebgott, R. Prost, and D. Friboulet, “Pre-beamformed RF signal reconstruction in medical ultrasound using compressive sensing,” *Ultrasonics*, 2012.
- [7] O. Lorintiu, H. Liebgott, M. Alessandrini, O. Bernard, and D. Friboulet, “Compressed sensing reconstruction of 3D ultrasound data using dictionary learning and line-wise subsampling,” *IEEE Transactions on Medical Imaging*, vol. 34, no. 12, pp. 2467–2477, 2015.
- [8] N. Wagner, Y. C. Eldar, and Z. Friedman, “Compressed beamforming in ultrasound imaging,” *IEEE Transactions on Signal Processing*, vol. 60, no. 9, pp. 4643–4657, 2012.
- [9] C. Quinsac, A. Basarab, D. Kouamé, and J.-M. Grégoire, “3D compressed sensing ultrasound imaging,” in *Ultrasonics Symposium (IUS), 2010 IEEE*. IEEE, 2010, pp. 363–366.
- [10] C. Schretter, S. Bundervoet, D. Blinder, A. Doooms, J. Dhooge, and P. Schelkens, “Ultrasound imaging from sparse RF samples using

- system point spread functions,” *IEEE Transactions on Ultrasonics, Ferroelectrics, and Frequency Control*, vol. 65, no. 3, pp. 316–326, 2018.
- [11] M. Vetterli, P. Marziliano, and T. Blu, “Sampling signals with finite rate of innovation,” *IEEE Trans. Signal Process.*, vol. 50, no. 6, pp. 1417–1428, 2002.
- [12] A. Krizhevsky, I. Sutskever, and G. E. Hinton, “Imagenet classification with deep convolutional neural networks,” in *Advances in neural information processing systems*, 2012, pp. 1097–1105.
- [13] K. He, X. Zhang, S. Ren, and J. Sun, “Deep residual learning for image recognition,” in *Proceedings of the IEEE Conference on Computer Vision and Pattern Recognition*, 2016, pp. 770–778.
- [14] Y. Ganin, E. Ustinova, H. Ajakan, P. Germain, H. Larochelle, F. Laviolette, M. Marchand, and V. Lempitsky, “Domain-adversarial training of neural networks,” *Journal of Machine Learning Research*, vol. 17, no. 59, pp. 1–35, 2016.
- [15] O. Ronneberger, P. Fischer, and T. Brox, “U-net: Convolutional networks for biomedical image segmentation,” in *International Conference on Medical Image Computing and Computer-Assisted Intervention*. Springer, 2015, pp. 234–241.
- [16] K. Zhang, W. Zuo, Y. Chen, D. Meng, and L. Zhang, “Beyond a Gaussian denoiser: Residual learning of deep CNN for image denoising,” *arXiv preprint arXiv:1608.03981*, 2016.
- [17] J. Kim, J. K. Lee, and K. M. Lee, “Accurate image super-resolution using very deep convolutional networks,” in *Proceedings of the IEEE Conference on Computer Vision and Pattern Recognition*, 2016, pp. 1646–1654.
- [18] E. Kang, J. Min, and J. C. Ye, “A deep convolutional neural network using directional wavelets for low-dose x-ray ct reconstruction,” *Medical Physics*, vol. 44, no. 10, 2017.
- [19] H. Chen, Y. Zhang, M. K. Kalra, F. Lin, Y. Chen, P. Liao, J. Zhou, and G. Wang, “Low-dose ct with a residual encoder-decoder convolutional neural network,” *IEEE transactions on medical imaging*, vol. 36, no. 12, pp. 2524–2535, 2017.
- [20] E. Kang, W. Chang, J. Yoo, and J. C. Ye, “Deep convolutional framelet denoising for low-dose CT via wavelet residual network,” *IEEE Transactions on Medical Imaging*, vol. 37, no. 6, pp. 1358–1369, 2018.
- [21] H. Chen, Y. Zhang, W. Zhang, P. Liao, K. Li, J. Zhou, and G. Wang, “Low-dose CT via convolutional neural network,” *Biomedical Optics Express*, vol. 8, no. 2, pp. 679–694, 2017.
- [22] J. Adler and O. Öktem, “Learned primal-dual reconstruction,” *IEEE Transactions on Medical Imaging (in press)*, 2018.
- [23] J. M. Wolterink, T. Leiner, M. A. Viergever, and I. Išgum, “Generative adversarial networks for noise reduction in low-dose CT,” *IEEE Transactions on Medical Imaging*, vol. 36, no. 12, pp. 2536–2545, 2017.
- [24] K. H. Jin, M. T. McCann, E. Froustey, and M. Unser, “Deep convolutional neural network for inverse problems in imaging,” *IEEE Transactions on Image Processing*, vol. 26, no. 9, pp. 4509–4522, 2017.
- [25] Y. Han and J. C. Ye, “Framing U-Net via deep convolutional framelets: Application to sparse-view CT,” *IEEE Transactions on Medical Imaging*, vol. 37, no. 6, pp. 1418–1429, 2018.
- [26] S. Wang, Z. Su, L. Ying, X. Peng, S. Zhu, F. Liang, D. Feng, and D. Liang, “Accelerating magnetic resonance imaging via deep learning,” in *Biomedical Imaging (ISBI), 2016 IEEE 13th International Symposium on*. IEEE, 2016, pp. 514–517.
- [27] K. Hammernik, T. Klatzer, E. Kobler, M. P. Recht, D. K. Sodickson, T. Pock, and F. Knoll, “Learning a variational network for reconstruction of accelerated MRI data,” *Magnetic resonance in medicine*, vol. 79, no. 6, pp. 3055–3071, 2018.
- [28] J. Schlemper, J. Caballero, J. V. Hajnal, A. N. Price, and D. Rueckert, “A deep cascade of convolutional neural networks for dynamic MR image reconstruction,” *IEEE Transactions on Medical Imaging*, vol. 37, no. 2, pp. 491–503, 2018.
- [29] B. Zhu, J. Z. Liu, S. F. Cauley, B. R. Rosen, and M. S. Rosen, “Image reconstruction by domain-transform manifold learning,” *Nature*, vol. 555, no. 7697, p. 487, 2018.
- [30] D. Lee, J. Yoo, S. Tak, and J. Ye, “Deep residual learning for accelerated MRI using magnitude and phase networks,” *IEEE Transactions on Biomedical Engineering*, 2018.
- [31] Y. LeCun, Y. Bengio, and G. Hinton, “Deep learning,” *Nature*, vol. 521, no. 7553, p. 436, 2015.
- [32] D. Allman, A. Reiter, and M. A. L. Bell, “A machine learning method to identify and remove reflection artifacts in photoacoustic channel data,” in *2017 IEEE International Ultrasonics Symposium (IUS)*, Sept 2017, pp. 1–4.
- [33] A. Luchies and B. Byram, “Deep neural networks for ultrasound beam-forming,” in *2017 IEEE International Ultrasonics Symposium (IUS)*, Sept 2017, pp. 1–4.
- [34] K. H. Jin, Y. S. Han, and J. C. Ye, “Compressive dynamic aperture b-mode ultrasound imaging using annihilating filter-based low-rank interpolation,” in *2016 IEEE 13th International Symposium on Biomedical Imaging (ISBI)*. IEEE, 2016, pp. 1009–1012.
- [35] K. H. Jin, D. Lee, and J. C. Ye, “A general framework for compressed sensing and parallel mri using annihilating filter based low-rank hankel matrix,” *IEEE Transactions on Computational Imaging*, vol. 2, no. 4, pp. 480–495, 2016.
- [36] D. Lee, K. H. Jin, E. Y. Kim, S.-H. Park, and J. C. Ye, “Acceleration of MR parameter mapping using annihilating filter-based low rank hankel matrix (ALOHA),” *Magnetic Resonance in Medicine*, vol. 76, no. 6, pp. 1848–1864, 2016.
- [37] J. Lee, K. H. Jin, and J. C. Ye, “Reference-free single-pass EPI Nyquist ghost correction using annihilating filter-based low rank Hankel matrix (ALOHA),” *Magnetic Resonance in Medicine*, vol. 76, no. 6, pp. 1775–1789, 2016.
- [38] J. C. Ye, J. M. Kim, K. H. Jin, and K. Lee, “Compressive sampling using annihilating filter-based low-rank interpolation,” *IEEE Transactions on Information Theory*, vol. 63, no. 2, pp. 777–801, Feb. 2017.
- [39] J. P. Haldar, “Low-Rank Modeling of Local k -Space Neighborhoods (LORAKS) for Constrained MRI,” *IEEE transactions on medical imaging*, vol. 33, no. 3, pp. 668–681, 2014.
- [40] J. C. Ye, Y. Han, and E. Cha, “Deep convolutional framelets: A general deep learning framework for inverse problems,” *SIAM Journal on Imaging Sciences*, vol. 11, no. 2, pp. 991–1048, 2018.
- [41] A. Misaridis, “Ultrasound imaging using coded signals,” Ph.D. dissertation, Technical University of Denmark, Department of Electrical Engineering, 2001.
- [42] D. P. Shattuck, M. D. Weinshenker, S. W. Smith, and O. T. von Ramm, “Explosocan: A parallel processing technique for high speed ultrasound imaging with linear phased arrays,” *The Journal of the Acoustical Society of America*, vol. 75, no. 4, pp. 1273–1282, 1984.
- [43] O. T. Von Ramm, S. W. Smith, and H. G. Pavy, “High-speed ultrasound volumetric imaging system. II. parallel processing and image display,” *IEEE transactions on ultrasonics, ferroelectrics, and frequency control*, vol. 38, no. 2, pp. 109–115, 1991.
- [44] K. H. Jin and J. C. Ye, “Annihilating filter-based low-rank Hankel matrix approach for image inpainting,” *IEEE Transactions on Image Processing*, vol. 24, no. 11, pp. 3498–3511, 2015.
- [45] K. H. Jin, J.-Y. Um, D. Lee, J. Lee, S.-H. Park, and J. C. Ye, “Mri artifact correction using sparse+ low-rank decomposition of annihilating filter-based hankel matrix,” *Magnetic resonance in medicine*, vol. 78, no. 1, pp. 327–340, 2017.
- [46] Y. Han and J. C. Ye, “ k -space deep learning for accelerated MRI,” *arXiv preprint arXiv:1805.03779*, 2018.
- [47] D. D. Lee and H. S. Seung, “Unsupervised learning by convex and conic coding,” in *Advances in neural information processing systems*, 1997, pp. 515–521.
- [48] —, “Learning the parts of objects by non-negative matrix factorization,” *Nature*, vol. 401, no. 6755, p. 788, 1999.
- [49] —, “Algorithms for non-negative matrix factorization,” in *Advances in neural information processing systems*, 2001, pp. 556–562.
- [50] M. Abadi, P. Barham, J. Chen, Z. Chen, A. Davis, J. Dean, M. Devin, S. Ghemawat, G. Irving, M. Isard *et al.*, “Tensorflow: A system for large-scale machine learning,” in *OSDI*, vol. 16, 2016, pp. 265–283.
- [51] A. Vedaldi and K. Lenc, “Matconvnet: Convolutional neural networks for matlab,” in *Proceedings of the 23rd ACM international conference on Multimedia*. ACM, 2015, pp. 689–692.
- [52] X. Glorot and Y. Bengio, “Understanding the difficulty of training deep feedforward neural networks,” in *Proceedings of the Thirteenth International Conference on Artificial Intelligence and Statistics*, 2010, pp. 249–256.
- [53] R. M. Rangayyan, *Biomedical Image Analysis*, ser. Biomedical Engineering, M. R. Neuman, Ed. Boca Raton, Florida: CRC Press, 2005.
- [54] Z. Wang, A. C. Bovik, H. R. Sheikh, and E. P. Simoncelli, “Image quality assessment: from error visibility to structural similarity,” *IEEE Transactions on Image Processing*, vol. 13, no. 4, pp. 600–612, April 2004.